

3D Photometric Cosmic Shear

T. D. Kitching^{1*}, A. F. Heavens¹ & L. Miller²

¹*SUPA, Institute for Astronomy, School of Physics, University of Edinburgh, Royal Observatory, Blackford Hill, Edinburgh, EH9 3HJ, U.K.*

²*Department of Physics, Oxford University, Keble Road, Oxford, OX1 3RH, U.K.*

ABSTRACT

Here we present a number of improvements to weak lensing 3D power spectrum analysis, 3D cosmic shear, that uses the shape and redshift information of every galaxy to constrain cosmological parameters. We show how photometric redshift probability distributions for individual galaxies can be directly included in this statistic with no averaging. We also include the Limber approximation, considerably simplifying full 3D cosmic shear analysis, and we investigate its range of applicability. Finally we show the relationship between weak lensing tomography and the 3D cosmic shear field itself; the steps connecting them being the Limber approximation, a harmonic-space transform and a discretisation in wavenumber. Each method has its advantages: 3D cosmic shear analysis allows straightforward inclusion of all relevant modes, thus ensuring minimum error bars, and direct control of the range of physical wavenumbers probed, to avoid the uncertain highly nonlinear regime. On the other hand, tomography is more convenient for checking systematics through direct investigation of the redshift dependence of the signal. Finally, for tomography, we suggest that the angular modes probed should be redshift-dependent, to recover some of the 3D advantages.

Key words: Cosmology: theory – large-scale structure of Universe

1 INTRODUCTION

Cosmology is faced with a standard model that contains two dominant unknown components (dark energy and dark matter) and two untested assumptions (that general relativity applies on large scales and that there was an inflationary period in the early Universe). In order to move forward from this unsatisfactory situation the need for high precision methods, which exhibit a strong statistical signal to cosmological parameters (those that describe the standard model or deviations from it) to allow various models to be compared with a high discriminatory power, is obvious.

It has become clear that 3D cosmic shear (Heavens, 2003; Castro, Heavens, Kitching, 2005; Heavens et al., 2006; Kitching et al., 2007) and weak lensing tomography (Hu 1999; Amara & Refregier, 2007; Bernstein & Jain, 2006), in which galaxy redshifts and the weak lensing shear distortion are used simultaneously in the signal, is an approach which is remarkably sensitive to cosmological parameters through both the growth of structure and the geometric behaviour of the lensing effect itself. For example neutrino mass (Hannestad et al., 2007; Kitching, Heavens, Verde, 2007; de Bernardis et

al., 2009; Jimenez et al., 2010), modified gravity (Thomas et al., 2008; Heavens, Kitching, Verde, 2008), dark matter (Camera et al., 2010; see Massey et al., 2010 for a recent review). In particular, given a current focus on dark energy (Albrecht et al., 2006; Peacock & Schneider, 2006) as the point in which we may find a departure from our standard model, it has been shown (and is widely accepted) that 3D cosmic shear has the potential to place tight constraints on the equation of state of dark energy.

This article is concerned with the techniques outlined in Heavens (2003), Heavens et al. (2006) and Kitching et al. (2007) whereby the 3D shear field (a function of redshift and angle) is treated in its entirety. In this approach the 3D shear power spectrum is reconstructed using spherical harmonics and the cosmological signal is found in the covariance of the coefficients. This is an alternative to weak lensing tomography where the 3D shear field is binned and projected in redshift space to produce a series of 2D projections, from which the auto- and cross-power spectra can be calculated (e.g. Hu 1999; Amara & Refregier, 2007; Schrabback et al., 2009).

3D cosmic shear has some advantage over tomography in that no binning is required, avoiding its consequent loss of information. One of the purposes of this article is to explore

* tdk@roe.ac.uk

the relationship between 3D cosmic shear and tomography. 3D cosmic shear in principle allows a full sky reconstruction including the effects of sky curvature. Individual pairs of galaxies in redshift can be excluded from the estimator directly (to reduce intrinsic alignment contamination; King & Schneider, 2002; Heymans & Heavens, 2003) and since every galaxy contributes directly and individually to the signal information such as the probability distribution in redshift of individual galaxies can be included in the estimator.

This final point, the inclusion of individual redshift probabilities, has been alluded to but has not been implemented up until now in 3D cosmic shear. Previously the inclusion of photometric redshift uncertainties has been through the use of the average photometric redshift error distribution at each redshift. We will show that this approach can lead to a mis-estimate of cosmological errors, and introduces small biases in cosmological parameter.

We will also present a Limber approximation of the full 3D shear field and show that for the range of (radial and azimuthal) modes which are sensitive to cosmological information the approximation is very good. This approximation vastly simplifies the theoretical computation of the 3D covariance, making it as simple as tomography to apply. We also explicitly derive the weak lensing tomography power spectra from the full 3D shear field, showing that these are related by two approximations (the Limber approximation, and the binning approximation), and demonstrate that tomography provides a sampling of the physical wavenumber space which is ℓ - and bin-dependent.

This paper is organised as follows. In Section 2 we will review the 3D cosmic shear formalism and show how photometric redshift information from individual galaxies can be explicitly included, using Fisher matrices we will investigate the impact on parameter error and bias. In Sections 3 and 4 we will present several approximations of the 3D shear field, using the Limber approximation. We discuss results in Section 5.

2 PHOTOMETRIC 3D SHEAR ESTIMATOR

3D cosmic shear decomposes the 3D shear field (a function of angular and radial position) using spherical harmonics (see Heavens, 2003; Castro, Heavens, Kitching, 2006; Heavens et al., 2006). Using the flat sky approximation we replace spherical harmonics with exponential functions, and assuming the Universe is flat we replace the more general ultra-spherical Bessel functions by spherical Bessel functions, a 3D shear estimator can be written, by summing over galaxies

$$\hat{\gamma}_i(k, \ell) = \sqrt{\frac{2}{\pi}} \sum_g \gamma_i^g j_\ell(k r_0^g) e^{-i\ell \cdot \theta^g} W(r_0^g) \quad (1)$$

where γ_i^g is the i^{th} shear component for each galaxy g at angular position θ and radial position r_0^g , which is obtained

from the photometric redshift assuming a fiducial cosmology. $W(r)$ is an optional weight which we set to $W = 1$ for clarity in the remainder of this article, we note here that there may exist optimal weights, particularly for constraining a certain cosmological parameter set. r_0^g is a distance, not a redshift, so to convert from some data (spectra/photometry \rightarrow redshifts) requires the assumption of a cosmology – however as shown in Kitching et al. (2007) this assumption is benign. Note that the transform convention of Castro et al. (2005) includes an extra factor of k , which we omit. The result of this expansion is a set of four 3D data vectors that are functions of angular wavenumber ($\ell = 2\pi/\theta$) and radial wavenumber and a real and imaginary part of γ_1 and γ_2 . Note that the behaviour of the Bessel functions (that $j_\ell(x) \ll 1$ for $x \ll \ell$) ensures that a mode of radial wavenumber k also has no transverse power with smaller wavelengths, so we are justified in identifying k as a physical wavenumber in 3D space. The assumption of a flat sky (resulting in an exponential in place of Y_ℓ^m above) can be relaxed (see Castro et al., 2005), resulting in a covariance of this estimator that is similar to the one that we derive below, we leave a full investigation of this for a future article. The assumption of a flat Universe (resulting in Bessel functions in place of ultra-spherical Bessel functions) can also be relaxed, for computational and notational convenience we use Bessel functions in this article and take small perturbations about this model.

Since the mean of the estimators is zero we use the covariance (Tegmark, Taylor & Heavens, 1997) of the estimator to constrain cosmology. In Appendix A we derive an expression for the expected covariance of the 3D shear estimators keeping track of any sum over galaxies. We may write the components of the shear estimator by $\hat{\gamma}_1(k, \ell) = \frac{1}{2} (\hat{\Gamma}_{11} - \hat{\Gamma}_{22})$ and $\hat{\gamma}_2(k, \ell) = \hat{\Gamma}_{12} = \hat{\Gamma}_{21}$, where the Γ terms are defined in terms of the lensing potential ϕ by $\Gamma_{ij} = \partial_i \partial_j \phi$, and have covariance

$$\begin{aligned} C_{ij,\ell}^{3D}(k_1, k_2) &= \langle \hat{\Gamma}_{ij}(k_1, \ell) \hat{\Gamma}_{ij}^*(k_2, \ell) \rangle = \\ &\Delta\Omega \ell_i^2 \ell_j^2 \left(\frac{2}{\pi}\right)^2 \left(\frac{4}{c^2}\right) A^2 \sum_g \sum_h j_\ell(k_1 r_0^g) j_\ell(k_2 r_0^h) \\ &\int_0^{r_0^g} dr' \int_0^{r_0^h} dr'' F_K(r^g, r') F_K(r^h, r'') \\ &\int \frac{dk'}{k'^2} \frac{1}{a(r')a(r'')} j_\ell(k' r') j_\ell(k' r'') \sqrt{P(k'; r') P(k'; r'')} \end{aligned} \quad (2)$$

$F_k(r, r') = S_k(r - r') / [S_k(r) S_k(r')]$ ($S_k = \sinh(k)$, $k, \sin(k)$ for open, flat or closed geometries so $F_k(r, r') = (r - r')/rr'$ for a flat universe), $a(r) = 1/[1 + z(r)]$ is the scale factor and $P(k; r)$ is the 3D matter power spectrum. The prefactors to this expression are $\Delta\Omega$ the dimensionless area of the survey, $A = 3\Omega_m H^2/2$ where Ω_m is the present dimensionless matter density and H is the present Hubble expansion rate. The $\ell_i^2 \ell_j^2$ is a factor that is introduced as a result of the derivative taken when transforming the lensing potential to the shear (see Heavens et al., 2006 and Kitching et al., 2007). The ℓ modes are uncorrelated due to the assumption of isotropy. To fully describe a non-Gaussian random field higher order potential correlations are required (see Munshi et al., 2010). The r_0^g and r_0^h are calculated from photometric redshifts assuming a fiducial model, where the r^g and r^h are

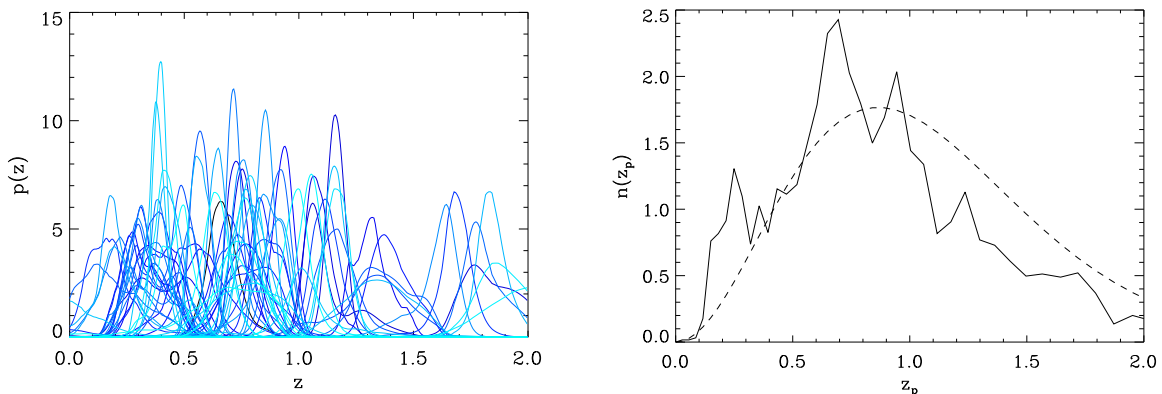


Figure 1. Left panel: a sample of 50 redshift distributions from the sample used (from Bordoloi et al., 2009). Right panel: the $n(z_p) = \sum_g p(z_p)$ from the total set of $p(z)$, the dashed line shows the functional form for $n(z) \propto z^2 \exp[-(1.4z/z_m)^{1.5}]$ from Taylor et al., (2007) with $z_m = 1.0$ for comparison.

their true values. This expression is one of the main results of this article.

In making any parameter error forecasts we will use the Fisher matrix formalism (Tegmark, Taylor, Heavens, 1997) and assume Gaussian likelihood surfaces, and Gaussian distributions for the data. For 3D cosmic shear the Fisher matrix was introduced in Heavens (2003) and examined in more detail in Heavens et al., (2006) and Kitching et al., (2007). Since we are assuming that the parameters affect the covariance, not the mean, the Fisher matrix is given by

$$F_{\alpha\beta} = \frac{g}{2} \int d\phi_\ell \int d\ell \text{Tr}[C_\ell^{-1} C_{\ell,\alpha} C_\ell^{-1} C_{\ell,\beta}] \quad (3)$$

where we include an integral over ℓ -space¹ which includes a density of states in ℓ -space, $g = \text{Area}/(2\pi)^2$ (see Appendix B of Kitching et al., 2007). A comma represents a derivative with respect to parameter α or β . The covariance C is a contribution of signal terms and (shot) noise terms $C = C^{\text{signal}} + C^{\text{noise}}$, where the signal is defined in equation (2) (we have suppressed the notation $C_{ij,\ell}^{3D}(k_1, k_2) \rightarrow C_\ell$ for clarity in equation 3). The shot noise covariance matrix used is the same as that in Heavens et al., (2006).

Throughout we will use the parameter set (with fiducial values) : $\Omega_m(0.3)$, $\Omega_{de}(0.7)$, $w_0(-0.95)$, $w_a(0.0)$, $h(0.71)$, $\Omega_b(0.045)$, $\sigma_8(0.8)$ and $n_s(1.0)$. We use the expansion of the dark energy equation of state as introduced in Chevallier & Polarski (2001) and Linder (2003), we include generally

curved geometries where $\Omega_k = 1 - \Omega_m - \Omega_{de}$ ². Our matter power spectrum is constructed using the Eisenstein & Hu (1999) transfer functions, with baryon wiggles, and employ the Smith et al. (2003) non-linear correction; for curved cosmologies with varying $w(z)$ we use the iCosmo (Refregier et al., 2008) interpolation scheme (also discussed in Schrabback et al., 2009).

Throughout we do not include any systematics effects in the predicted parameters errors. However we note that the impact from all primary systematics (photometric redshift calibration, intrinsic alignments and shape measurement error) should be at most a factor of $\sqrt{2}$ on cosmological parameters (Kitching et al., 2008) in a realistic self-calibration regime using parameterised systematic functions. Using non-parametric approaches may degrade results further, but as shown in Kitching & Taylor (2010) and Kitching et al. (2009), using tomographic analyses, the overall cosmological impact is not severe.

We assume a fiducial survey configuration of 20,000 square degrees, with a surface number density of 35 galaxies per square arcminute and an intrinsic ellipticity dispersion of 0.3. Where we do not use direct photometric redshift probabilities we will use a redshift distribution of galaxies $n(z) \propto z^2 \exp[-(1.4z/z_m)^{1.5}]$ given in Taylor et al., (2007) with a median redshift of $z_m = 1$ and a Gaussian redshift dispersion with a redshift error $\sigma_z(z) = 0.03(1+z)$. This survey configuration is similar to the proposed Euclid wide survey (Refregier et al., 2010). Throughout we use a maximum azimuthal wavenumber of $\ell_{\text{max}} = 5000$ and a maximum radial wavenumber of $k_{\text{max}} = 1.5h\text{Mpc}^{-1}$ to avoid the highly non-linear regime where theoretical predictions for the power spectrum may be unsound (e.g. Rudd et al., 2008; Joudaki et al., 2009).

¹ The density of states accounts for correlations between modes arising from partial sky coverage, equivalent to the f_{sky} approach of many papers. Note that the insensitivity to large-scale modes, which is also a consequence of using a patch of sky, needs to be treated by a cut on ℓ . The Fisher matrix approach assumes the data are Gaussian; see Munshi et al., (2010) for an investigation of non-Gaussianity in 3D shear.

² In this case ultra spherical Bessel functions should be used, but as pointed out in Kitching et al. 2007 in the $\ell \gg 1$ and $k \gg (\text{curvature})^{-1}$ regime the use of the $j_\ell(kr)$ is well justified.

2.1 Including Photometric Redshifts

For the depth of surveys required for optical weak lensing, it is impractical to obtain spectroscopic redshifts, so photometric redshifts z_p are obtained, typically from broad-band photometry. Some photo-z codes return a complete posterior probability distribution for the redshift, given the photometry, and the purpose of this section is to show that this individual information can be used when it exists. Since it uses all the information available, it should yield a more accurate covariance matrix than the alternative of reducing the redshift distributions to a simpler $\bar{p}(z|z_p)$; the form of p may be arbitrary (and include for example outliers), but its distribution is assumed in the alternative approach to be the same for all galaxies with the same photometric redshift. Note that, although a full posterior redshift distribution may be returned, we still do have to identify a unique photo-z for each galaxy, to provide an r_0^g to insert into the spherical Bessel function weighting.

To include galaxy photometric redshift errors we integrate over the posterior redshift distribution for each galaxy. We write this as $p_g(z|z_g)$ as a shorthand for the redshift probability distribution given all the photometric information available for galaxy g :

$$C_{ij,\ell}^{3D}(k_1, k_2) = \Delta\Omega\ell_i^2\ell_j^2\frac{4}{\pi^2c^2}A^2\sum_g\sum_h[j_\ell(k_1r_0^g)j_\ell(k_2r_0^h)] \\ \int dz'p_g(z'|z_g)\int dz''p_h(z''|z_h) \\ \int_0^{r'}d\tilde{r}'\int_0^{r''}d\tilde{r}''F_K(r',\tilde{r}')F_K(r'',\tilde{r}'') \\ \int \frac{dk'}{k'^2}\frac{1}{a(\tilde{r}')a(\tilde{r}'')}j_\ell(k'\tilde{r}')j_\ell(k'\tilde{r}'')\sqrt{P(k';\tilde{r}')P(k';\tilde{r}'')}, \quad (4)$$

where $r' = r(z')$. This is the covariance of the full 3D shear field constructed only from a sum over the individual tracer galaxy population, and including all uncertainty that may be present from photometric redshift estimates.

In this formalism we can retain individual posteriors. Since we do not want the data vector to depend on the cosmological parameters (and consequently violating the conditions of the Fisher matrix analysis), we must assume a fiducial cosmology to translate a photo-z to a distance r_0^g . However as long as this choice, for each galaxy, is the same as those used in the actual sum over data (equation 1) then the estimator will be unbiased.

For clarity we can re-express the covariance as series of matrices

$$C_{ij,\ell}^{3D}(k_1, k_2) = A^2\int \frac{dk'}{k'^2}G_\ell^D(k_1, k')G_\ell^D(k_2, k') \\ G_\ell^D(k_1, k') = \sum_g j_\ell(k_1r_0^g)\int dz'p_g(z'|z_g)U_\ell(r(z'), k') \\ = \int dz'\left[\sum_g j_\ell(k_1r_0^g)p_g(z'|z_g)\right]U_\ell(r(z'), k')$$

$$U_\ell(r(z'), k') = \int_0^{r(z')} d\tilde{r}\frac{F_K(r(z'), \tilde{r})}{a(\tilde{r})}j_\ell(k'\tilde{r})P^{\frac{1}{2}}(k'; \tilde{r}) \quad (5)$$

where $A^2 = \Delta\Omega\ell_i^2\ell_j^2\frac{4}{\pi^2c^2}A^2$. Equation (5) is a discrete case of the equations in Section 2.5 of Heavens et al. (2006). The ij refer to γ combinations (see Appendix A), not redshift bins – this is a continuous 3D estimator.

If we do not have individual posterior distributions, or wish to ignore the individual galaxy redshift error distributions, we can simplify $p_g(z|z_g)$ to a global $\bar{p}(z|z_p)$ so all galaxies at fixed photometric redshift are assumed to have the same distribution of true redshifts. In this regime the G matrix is modified only so that

$$G_\ell^C(k_1, k') = \int dz_p dz' j_\ell(k_1r(z_p))n(z_p)\bar{p}(z'|z_p)U_\ell(r(z'), k') \quad (6)$$

where $\bar{p}(z|z_p)$ is the redshift probability distribution at photometric redshift z_p , and $n(z_p)$ is the number density of galaxies as a function of redshift. Equation (6) is in agreement with Castro et al. (2003) and Heavens et al. (2006).

By including the individual galaxies in equation (5) we automatically take into account all overlap between photometric redshift posteriors, all outliers in the sample and have the best estimate for the covariance of the data vector. Of course the outliers have only been properly accounted for only if the $p(z|z_p)$ is a correct estimate of the probability of a galaxy being an outlier; we leave an investigation into the effect of errors on the $p(z|z_p)$ for future study.

2.2 Forecasted Impact

To illustrate the effects, we use a sample of realistic photometric redshift probabilities $\{p(z_p)\}$ from Bordoloi et al. (2009), which are a simulated set of redshift probability distributions like those expected from Euclid. We show these in Figure 1. We use a representative sample of 3000 redshift distributions, for computational speed, which for a surface number density of $n_0 = 35$ per square arcmin represents a sample of galaxies from around 100 square arcmin. This is low compared to the expected number of galaxies in future surveys, however we use this sample as representative for the investigation of the approximations we highlighted in Section 2.1 – in fact with low(er) number statistics we may expect a larger deviation than in reality because the error on the mean will be larger (a $1/N$ effect). To match the total number to the surface density we multiply the signal covariance by an extra factor of $(n_0/3000)^2$ (and the noise by $n_0/3000$).

We consider two cases

- (i) First case, where we use the full covariance including

posteriors for the true redshifts³, equations (5).

(ii) Second case, where we make an approximation by summing the individual posteriors in photometric redshift intervals b , to find a global number density distribution as a function of redshift $\bar{p}(z|z_p) = \sum_{g,b} p_g(z|z_p)$, equation (6). This is one particular method of smoothing the redshift distribution, we would expect similar results with other smoothing kernels with a similar redshift scale. In this example we use 20 bins in z_p between the redshifts 0–2 (a step in redshift of 0.1).

We show the $n(z)$ from the sample of photometric redshift posteriors we use in Figure 1. In Figure 2 we show the impact on the 3D cosmic shear power spectra. The power spectra are a function of ℓ and two physical wavenumbers, hence we show the plane (k_1, k_2) for a series of ℓ modes, as well as the diagonal $C_\ell^{3D}(k, k)$. It can be seen that using an approximation of the redshift distribution can cause significant residuals in the power spectra, with residuals of order 0.01–1 over all scales. These residuals are most prominent at low- ℓ and small radial scales.

Using the Fisher matrix approach Figure 3 shows how the approximation of averaging the posteriors $\bar{p}(z|z_p)$ in photometric redshift, can affect cosmological parameter errors. In general the errors are degraded by averaging the individual galaxy posteriors $p_g(z|z_g)$ by a factor of 10–50%, and in some cases the parameter degeneracies are changed. This is a result of the individual $p_g(z|z_g)$ distributions explicitly including outlying and non-Gaussian behaviour on a galaxy-by-galaxy basis.

In making the approximation of $\bar{p}(z|z_p)$ the best fit cosmological parameter values may also be biased, as well as the errors being affected. In Appendix C we show how to calculate the bias in the Fisher matrix approximation for the case that the parameter dependency is in the covariance (this is a generalisation of the result of Knox et al., 1998). We find that the approximation made in this example introduces a negligible bias on all cosmological parameters : $\Omega_m(-3.0 \times 10^{-5})$, $\Omega_{de}(2.5 \times 10^{-4})$, $w_0(1.3 \times 10^{-4})$, $w_a(-1.2 \times 10^{-4})$, $h(5.2 \times 10^{-4})$, $\Omega_b(1.1 \times 10^{-6})$, $\sigma_8(7.3 \times 10^{-5})$ and $n_s(2.5 \times 10^{-4})$. We note that changes in the covariance only impact cosmological parameter biases if the change induced is similar to the effect of any cosmological parameter (see for example Kitching et al. 2009; form filling functions). In this case the changes in the covariance are large, but the changes are not similar to the effect of cosmological parameter so the biases are small. The amplitude of the bias will depend on the exact distribution and form of the posterior redshift distributions, here we use an example to introduce

the methodology, we leave a more detailed study for a future article.

For any given experiment, the exact degradation will be dependent on the exact galaxy survey and quality of photometric redshifts available.

Note that in Heavens et al. (2006) we made a further approximation by assuming that the $\bar{p}(z|z_p) = \bar{n}(z_p)p_{\text{Gauss}}(z|z_p)$, where $\bar{n}(z_p)$ is the number density of galaxies as a function of photometric redshift and $p_{\text{Gauss}}(z|z_p)$ is the normalised photometric redshift distribution at each redshift which we assumed to be a Gaussian at each redshift with a variance $\sigma_z(z_p)$.

3 LIMBER APPROXIMATION OF THE 3D SHEAR FIELD

We now investigate various approximations of the 3D shear field. From LoVerde & Afshordi (2008) the Limber approximation can be encapsulated in the following substitution

$$\lim_{\ell \rightarrow \infty} j_\ell(kr) \rightarrow \sqrt{\frac{\pi}{2(\ell + \frac{1}{2})}} \delta^D \left(kr - \left[\ell + \frac{1}{2} \right] \right), \quad (7)$$

where δ^D is the Dirac delta function. This is substituted into any integral or sum that the Bessel function appears; for example equations (5) and (6). We note that this does not explicitly convert a 3D wavevector into a 2D wavevector, $k = (k_x, k_y, k_z) \rightarrow (k_x, k_y)$ (which is explicit in an alternative and complementary derivation of the Limber approximation; Kaiser, 1998), but that this transformation is implicit when an integral over the delta function is performed.

By substituting this approximation into the matrices in equation (5) we can find an approximate expression of the covariance in the high ℓ limit. In this case the U matrix is modified to

$$U_\ell^{\text{Limber}}(r(z'), k') = \sqrt{\frac{\pi}{2(\ell + \frac{1}{2})}} \frac{F_K(r(z'), r_\nu)}{a(r_\nu)} P^{\frac{1}{2}}(k'; r_\nu) \quad (8)$$

where $r_\nu \equiv (\ell + \frac{1}{2})/k' < r(z')$.

In the individual redshift error case the G matrix is modified to

$$G_\ell^D(k_1, k') = \sqrt{\frac{\pi}{2(\ell + \frac{1}{2})}} \sum_{\{g: r_0^g = [\ell + \frac{1}{2}]/k_1\}} \int dz' p_g(z'|z^g) U_\ell^{\text{Limber}}(r(z'), k') \quad (9)$$

where each galaxy only contributes to a given combination of k_1 and ℓ set by its comoving distance $r_0^g = [\ell + \frac{1}{2}]/k_1$. We note that this equation in practice would require some binning in k and ℓ to obtain a finite number of galaxies in this sum.

³ In practice we have used redshift-binned true photometric redshift posteriors, using the resolution provided by Bordoloi et al. (2009), which was 5000 bins in redshift. This is sufficient to illustrate the method, since this is much larger than the number of $p(z)$ available. A binned description is not a limitation of this method – one could imagine a basis set description with no explicit redshift binning.

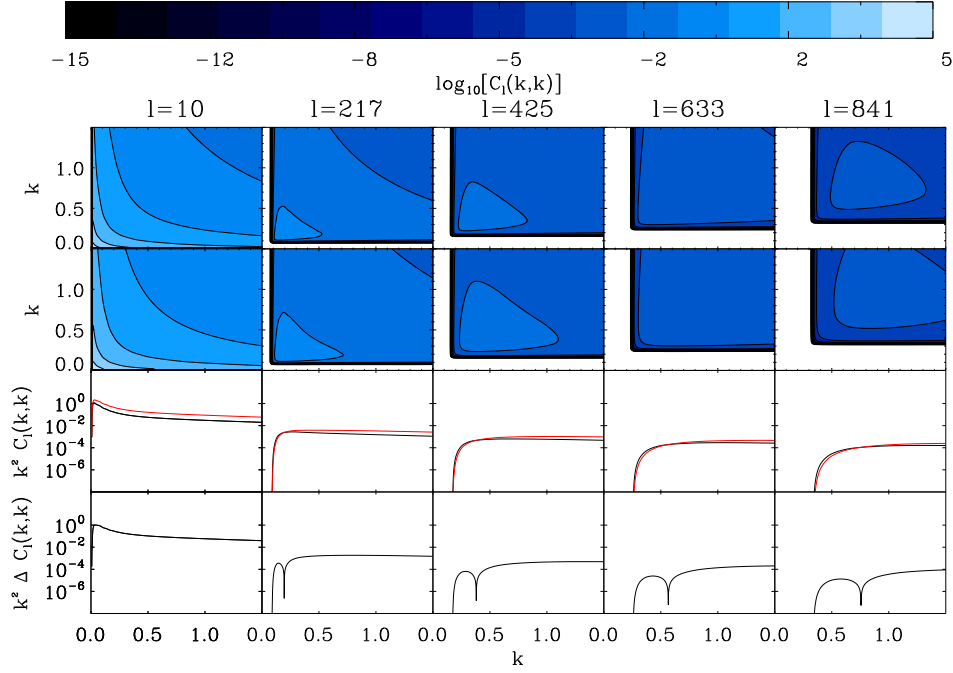


Figure 2. The 3D cosmic shear power spectra for the case where we use individual galaxy redshift distributions (upper panel), and using an approximation of the photometric probability distribution (second panels). The colour scale is shown in the bar above. The third set of panels shows the diagonal $C_\ell(k, k)$ of the full 3D power spectra for the full case (black lines) and for the approximation (red, dark grey lines). The bottom panels show the modulus of the difference in the diagonal elements. Rightwards of the cusp in the bottom panels the difference between the power spectra becomes negative. For a Euclid survey with Bordoloi et al., (2009) $p(z)$.

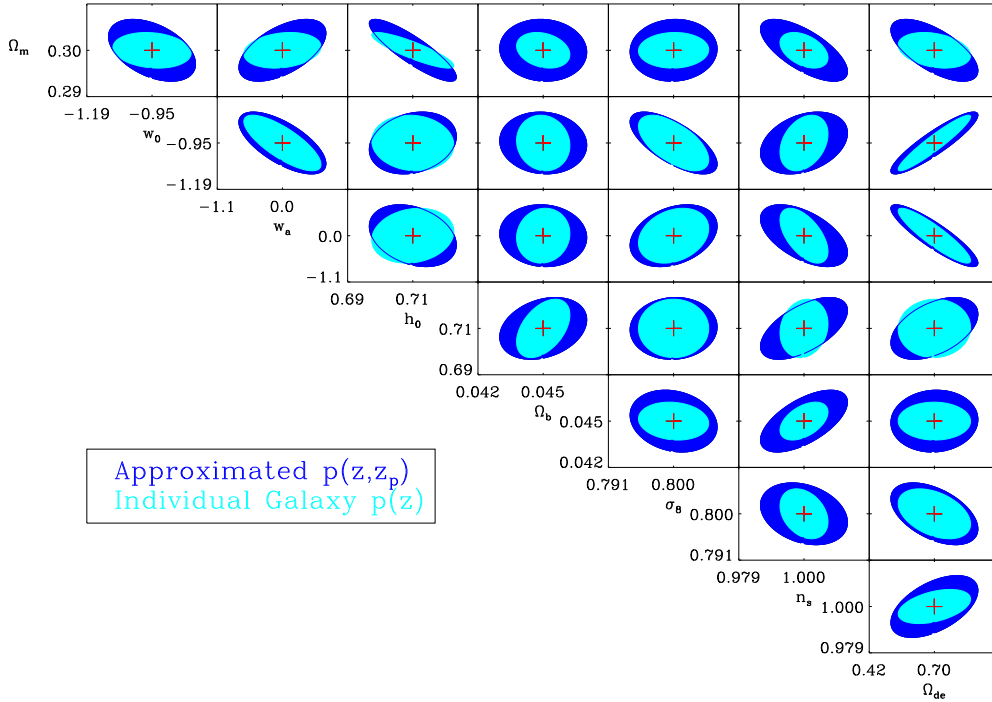


Figure 3. The Fisher matrix 2-parameter $1\text{-}\sigma$ constraints for the case where individual galaxy $p(z)$ are used and the approximation of using a summed, approximated global $\bar{p}(z|z_p)$. The central cross shows the fiducial values. This is for a Euclid survey (Refregier et al., 2010) using $p(z)$ from Bordoloi et al., (2009).

If a global error distribution is used, the G matrix is modified to

$$G_{\ell}^{C, \text{Limber}}(k_1, k') = \frac{1}{4\pi} n(z_{\nu}) \sqrt{\frac{\pi}{2(\ell + \frac{1}{2})}} \left(\frac{dz}{dr} \right)_{r_{\nu}} \int dz' \bar{p}(z'|z_{\nu}) U_{\ell}^{\text{Limber}}(r(z'), k'), \quad (10)$$

where $r_{\nu} = (\ell + \frac{1}{2})/k_1$ and z_{ν} are the photometric redshifts. The extra factor of $(\frac{dz}{dr})_{r_{\nu}}$ comes from the fact that the Bessel integral in equation (6) is over z not r .

By substituting the Bessel function approximation directly into the shear estimator, equation (1), it can be seen that the Limber approximation leads to an equivalence between the 3D k and ℓ values and the tomographic r and ℓ values. We will discuss the Limber approximation further in Section 4.

3.1 Convergence of the 3D Cosmic Shear

In Figure 4 we show the effect of the Limber approximation on the 3D cosmic shear power spectrum. We find that the Limber approximation is a remarkably good approximation to the full calculation for scales $\ell \gtrsim 100$, with residuals of $\sim 10^{-4}$ over all radial and azimuthal scales. The break at $k \sim \ell/r_{\text{max}}$ in the power spectra at each ℓ , caused by the Bessel function inequality $j_{\ell}(kr \lesssim \ell) \sim 0$, is reproduced through the inequality expressed after equation (8). For larger scales $\ell < 100$, there is a larger effect on the power spectrum.

In Figure 5 we show the effect of the Limber approximation on the expected cosmological errors. We find that in most parameter combinations some information is inevitably lost, through the largest scales being down weighted, the increase in errors is between 1–30% with an average increase of $\sim 10\%$.

We conclude that the Limber approximation is adequate for forecasting purposes, but if computer time allows, it is preferable to use the full expressions in data analysis.

4 TOMOGRAPHY FROM 3D COSMIC SHEAR

We now approximate the 3D shear field further and show how in the discrete real-space limit the tomographic power spectra can be reproduced. There have been some implicit references to this derivation, for example in Hu (1999), here we will show explicitly how the 3D shear field is related to the tomographic power spectrum.

Weak lensing tomography is a flavour of 3D weak lensing in which the angular and redshift information of each galaxy is used. The practical distinction between 3D cosmic shear and tomography is that tomography divides the redshift range into a series of bins and the 2D shear transform in each bin

is constructed. The auto (in a single bin) and cross (between bins) power spectra are used to constrain cosmological parameters.

Given the expressions in equations (8) to (10) we can now derive the weak lensing tomographic power spectra directly from the 3D shear field. In Appendix B we show how the 3D cosmic shear power spectrum using the Limber approximation can be written as

$$C_{\ell}^{3D, \text{Limber}}(k_1, k_2) = \frac{9\Omega_m^2 H^4}{4c^2} \int dr \frac{P(\ell/r; r)}{a^2(r)} \frac{\mathcal{W}(r_1, r)\mathcal{W}(r_2, r)}{r^2} \quad (11)$$

where we define a weight factor as

$$\mathcal{W}(r_i, r) = [n(r_i)r_i^2]r \int dr' \bar{p}(r') \frac{r - r'}{r'^2}, \quad (12)$$

where $r_i = \ell/k_i$ and $p(r[z]) = p(r[z]|r[z_p])$ is the redshift probability distribution, equivalent to $\bar{p}(z|z_p)$ in equation (6). We condense the notation here and in Appendix B to match the literature for the tomographic case. This is still a full 3D estimator where $r_1 = r(z_1)$ and $r_2 = r(z_2)$ can take any value, and in practice would be a sum over all galaxy pairs. This is a key result of this article, using only two integrals a full 3D shear power spectrum can be computed from the 3D matter power spectrum (as simple as the standard tomographic approximation).

Inspection of the previous equations shows that they are the usual expressions for the (auto- or cross-) power spectrum of tomography, from which we see that, under the Limber approximation, tomography samples discrete sets of physical wavenumbers, in an ℓ -dependent way: for shells at distances r_i , $k = \ell/r_i$.

In summary to convert from 3D cosmic shear to weak lensing tomography we see that the following three steps must be taken

- The **Limber approximation** must be applied to the full 3D shear estimator.
- **Fourier transform** the kernel integration from harmonic space to real space.
- **Discretisation** of physical modes through $k = \ell/r_i$.

The second step is benign in that no information should be lost, however the first and third steps do result in information loss (see Section 3.1 and 4.1). Interestingly for a specific redshift bin (r) and a specific azimuthal ℓ -mode the tomographic approximation only probes a single physical k -mode $k = \ell/r$ from the full 3D shear field; in contrast in 3D cosmic shear we have control over the k and ℓ modes over the whole redshift range.

Clearly by fixing the distances of the tomographic binning, we lose some flexibility over the physical wavenumbers probed, so there is a risk that either not all useful modes are included (increasing statistical errors), or that, for the nearby shells, the physical wavenumber range sampled ex-

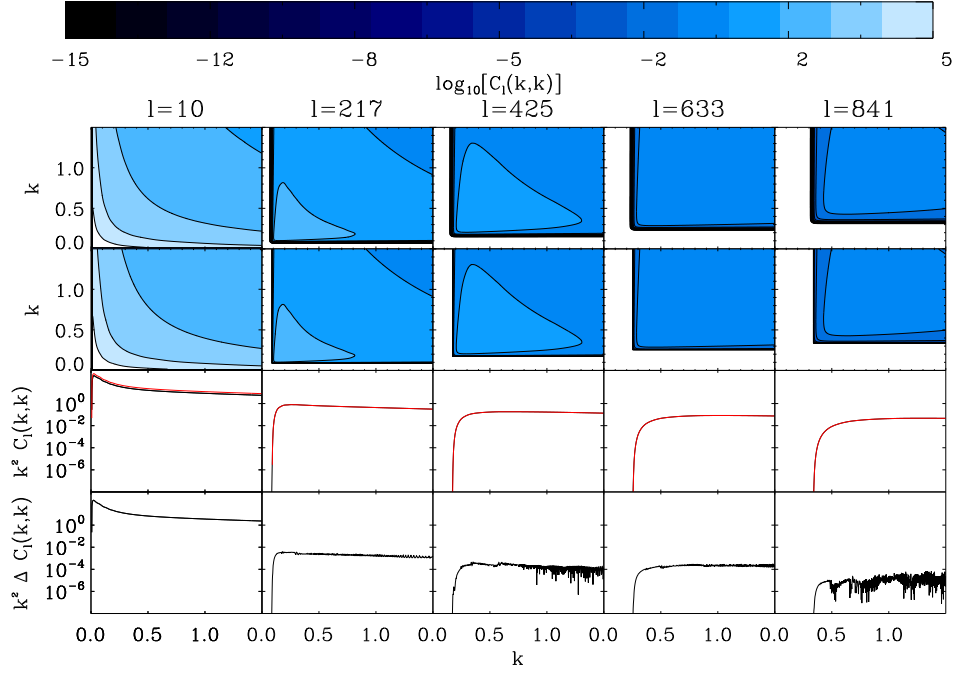


Figure 4. The 3D cosmic shear power spectra for the full 3D cosmic shear calculation (upper panels), and using the Limber approximation (second panels). The colour scale is shown in the bar above. The third set of panels show the diagonal $C_\ell(k, k)$ of the full 3D power spectra for the full calculation (black lines) and for the Limber approximation (red, dark grey lines). The bottom panels show the modulus of the difference in the diagonal elements. This is for a Euclid wide survey (Refregier et al., 2010).

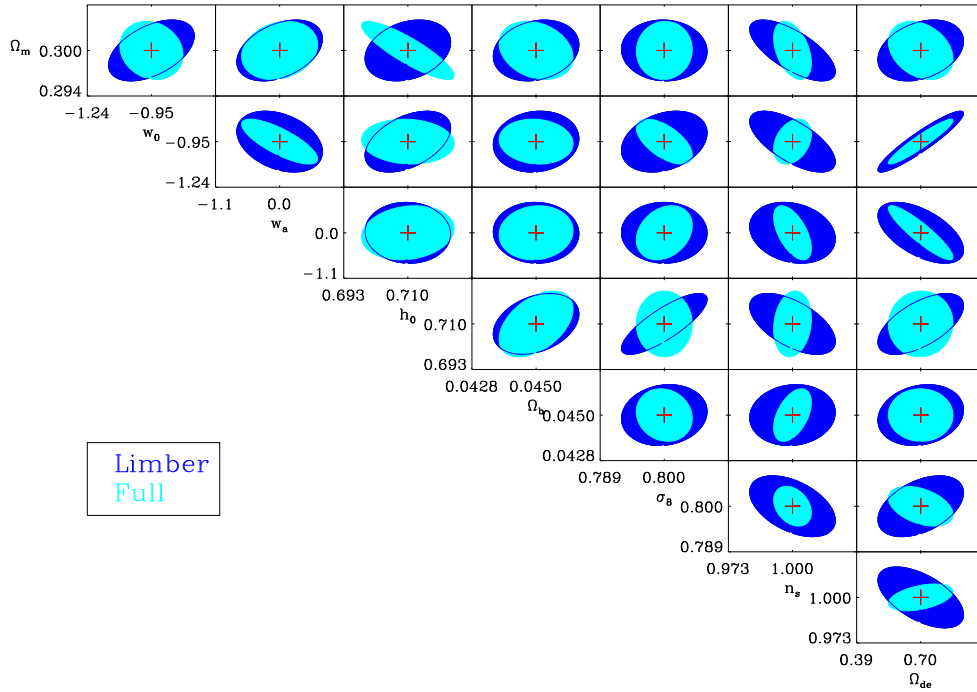


Figure 5. The Fisher matrix 2-parameter $1\text{-}\sigma$ constraints for the full 3D cosmic shear calculation and using the Limber approximation. Where filled the contours lie behind one another we outline the contours with a line. This is for a Euclid wide survey (Refregier et al., 2010).

tends to too high a value of k , where theoretical uncertainties become a potential source of systematic error. None of this is a fundamental problem for tomography; it simply requires that the ℓ range chosen should be redshift-dependent – increasing $\ell_{\max} = r[z]k_{\max}$ for the distant shells, and reducing it for nearby shells.

In a similar manner to Section 2 we can also keep the summation over galaxies explicit in the derivation of the tomographic power spectrum. In this case we have a very similar expression to equation (12), with the kernel functions are now replaced by

$$\begin{aligned} \mathcal{W}_{\text{individual}}(r, r_i) &= \sum_h r \int dr' p_h(r'|r^h) \frac{r-r'}{r'} \\ &= r \int dr' \left[\sum_h p_h(r'|r^h) \right] F_k(r', r), \end{aligned} \quad (13)$$

where we have summed over the set of galaxies $h = \{g : r_i - \Delta r \leq r \leq r_i + \Delta r\}$ within a bin defined by a width $2\Delta r$ centred on r_i . $p_h(r)$ is the redshift probability distribution for an individual galaxy within that bin.

4.1 Convergence of 3D shear

Here we investigate the predicted cosmological error constraints from 3D cosmic shear as more modes are included. We assume a survey configuration as given in Section 2, and restrict the analysis to the regime $\ell_{\max} = 5000$ and $k_{\max} = 1.5h\text{Mpc}^{-1}$ (with $N_{\text{modes}} = 1000$ k-modes evenly distributed over the range), we use the full posterior distributions from Bordoloi et al. (2009).

Figure 6 shows how the Fisher matrix errors vary, for w_0 and w_a as well as the dark energy Figure of Merit ($\text{FoM} = 1/\sqrt{F_{w_0 w_0}^{-1} F_{w_a w_a}^{-1} - (F_{w_0 w_a}^{-1})^2}$; Albrecht et al., 2006), as a function of the number of k modes sampled. We also show the 3D cosmic shear constraints using the Limber approximation. In Figure 6 we also show how the constraints in the (w_0, w_a) plane change as the number of modes is increased. We find that the cosmological constraints do not converge to the 3D (Limber) limit until the number of modes is $\gtrsim 800$ for low- ℓ modes.

We can understand the convergence if we consider that a separation of modes in k -space Δk for a given ℓ corresponds to physical separations Δr in the following way

$$\Delta k \simeq \frac{k_{\max}}{N_{\text{modes}}} \simeq \ell \frac{\Delta r}{r_1 r_2} \quad (14)$$

where $\Delta r = r_1 - r_2$ and $r_i = \ell/k_i$. We can use this as an approximate model to investigate the convergence properties.

We expect that convergence will occur in two regimes i) as radial modes enter the survey volume, ii) as radial modes become correlated due to the photometric/ $n(z)$ smoothing scale. To illustrate this we use equation (14). The depth of

the fiducial survey in this article is $\Delta r_{\text{survey}} \approx 3000h^{-1}\text{Mpc}$ (where $r_1 \sim 3000$ and $r_2 \sim 0$) such that $N_{\text{modes}} \approx 4500/\ell$. For $\ell = 150$ this should result in convergence at $N_{\text{modes, survey}} \approx 30$. The photometric/ $n(z)$ smoothing scale typically occurs at $\Delta r_{\text{photoz}} \approx 150h^{-1}\text{Mpc}$ in comoving coordinates in this case we see that $N_{\text{modes, photoz}} \approx 95,000/\ell$ from equation (14), for $\ell = 150$ this should create convergence at $N_{\text{modes}} \approx 600$. In Figure 7 we see that for all ℓ ranges the convergence occurs at the photometric/ $n(z)$ smoothing scale. For high- ℓ modes the survey convergence is not visible since $N_{\text{modes, survey}} \lesssim 10$. For low- ℓ modes the difference in the convergence regimes (30 and 600 k-bins) is clearly visible.

Note that this simple illustration is approximate since the radial smoothing scale is also a function of the lensing kernel. In Figure 7 we also show the the FoM convergence for $\sigma_z(z)/(1+z) = 0.01$ and 0.03 . In both cases the constraints improve sharply over the range 1–20 modes. This suggests that below $\sigma_z(z)/(1+z) \approx 0.03$ the radial smoothing scale is not significantly reduced, due to the lensing kernel. The change in $\sigma_z(z)$ has a sub-dominant effect on the FoM especially at low numbers of modes, which is in agreement with tomographic studies (e.g. Bridle & King, 2007) and in the 3D limit with Heavens et al. (2006).

We find that under the same survey assumptions, and a restriction to modes $\ell < 5000$, $k < 1.5h\text{Mpc}^{-1}$ that the 3D cosmic shear predictions agree very well with publicly available tomographic code (for example iCosmo; Refregier et al., 2008) and other tomographic studies (e.g. Amara & Refregier, 2007; Bernstein, 2009). We note however that typical tomographic studies use highly non-linear modes, $\ell \sim 10^4$ and $k \gg 1.5h\text{Mpc}^{-1}$, and consequently report tighter constraints.

We emphasise here that our results are consistent and complementary with tomographic studies. We find a convergence at the photometric smoothing scale. This is consistent with tomographic studies that find convergence at around 20 redshift bins which is also consistent with the photometric smoothing scale where $\Delta r \approx r_{\text{survey}}/r_{\text{photo}} \sim 3000/150 = 20$. We recommend that in any analysis both tomography and 3D cosmic shear should be performed

- Tomography allows one to explicitly scrutinise the redshift dependence of the signal.
- 3D cosmic shear allows for an explicit radial and azimuthal scale dependence to be investigated.

The redshift and scale dependence should be explicitly investigated by both methods respectively.

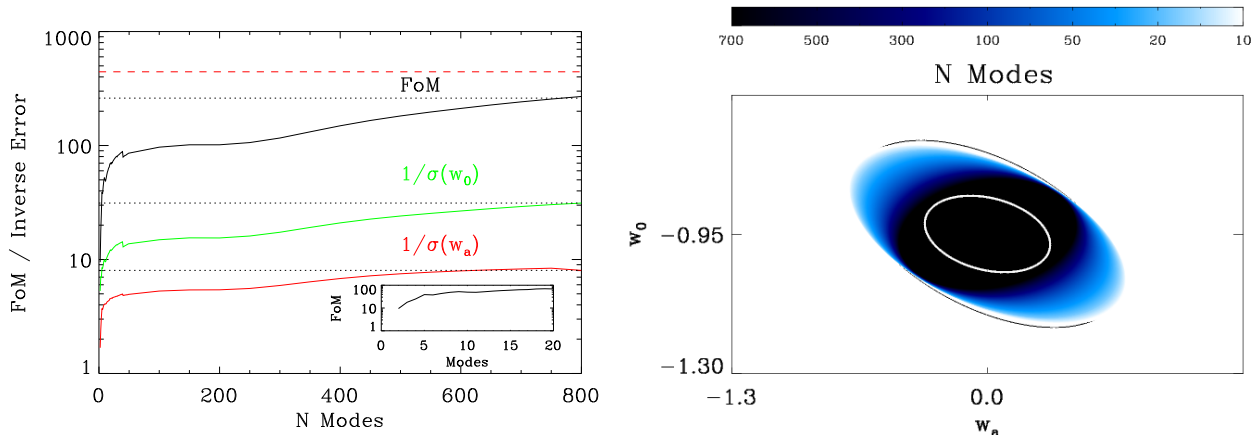


Figure 6. Mode convergence of 3D cosmic shear. For the 3D calculation we use the Limber approximation, equation (11). The left panel shows how the inverse errors ($1/\sigma$) for w_0 (middle green line), w_a (lower red line) as well as the dark energy Figure of Merit (upper black line) (Albrecht et al., 2006) vary with the number of k modes, for $\sigma_z(z)/(1+z) = 0.03$. The dotted horizontal lines show the 3D cosmic shear asymptotic predictions using the Limber approximation. The upper dashed (red) line shows the 3D cosmic shear prediction using the full (non-Limber) approximation. The inset shows the change in FoM over the range of 2 to 20 modes. The right panel shows the predicted $1-\sigma$ two-parameter constraints in the (w_0, w_a) plane, the colour represents the number of k -mode bins that we define in the colour bar, the central white ellipse shows the Limber approximation 3D cosmic shear constraints. This is for a Euclid wide survey (Refregier et al., 2010). We use $\ell_{\max} = 5000$ and $k_{\max} = 1.5h\text{Mpc}^{-1}$.

5 CONCLUSION

In this article we have developed the 3D cosmic shear technique in a number of ways. We have simplified the analysis using the Limber approximation, we have shown how to include individual posterior redshift probability distributions from photo-zs in the analysis. The technique presented here removes the need for any intermediate $p(z|z_p)$ estimation, allowing the estimator itself to become a direct function of the individual galaxy redshift probabilities.

Finally, we have clarified the relationship between 3D cosmic shear and tomography, and demonstrated that tomography essentially provides an ℓ - and shell-dependent sampling of physical wavenumber modes.

To study individual redshift errors, we used a mock catalogue of photometric redshift probabilities $p(z)$ from Bordoloi et al. (2009). We find that the cosmological errors can be mis-estimated by 10–50% by using an average $\bar{p}(z|z_p)$ in the estimator, but that biases on the cosmological parameters are negligible. In order to calculate the biases we have generalised the bias formalism introduced in Knox et al. (1998) to the case where the cosmological signal is in the covariance not the mean.

We have not investigated systematic effects that may be present in photometric redshift estimates. However we note that the outlier mitigation techniques and likelihood calibration methodology of Bordoloi et al. (2009) is relevant and should be used in conjunction with the techniques presented here, and leave this for future investigation. In addition we refer to Kitching et al. (2008) (systematic effects on 3D cosmic shear) where a factor of 2 degradation in FoM is expected as a result of the primary weak lensing systematics.

Using the extended Limber approximation of LoVerde & Afshordi (2008) we have found a much simpler expression for the 3D shear field in the high- ℓ regime. For angular wavenumbers $\ell \gtrsim 100$ the Limber approximation is essentially exact with a difference between the Limber and full calculation power spectra of $\lesssim 10^{-4}$; a fractional difference of $\lesssim 10^{-2}$.

Finally we explicitly derive the weak lensing tomographic power spectrum from the 3D cosmic shear field. We find that tomography essentially probes discrete sets of physical wavenumbers, which depend both on ℓ and on the distance to each individual tomographic bin.

The choice of tomographic bin positions constrains the 3D modes which can be analysed. The modes which should be probed have to satisfy several constraints: first, the maximum physical wavenumber should not be too high, to avoid the uncertain highly non-linear regime; secondly, as many modes as possible should be included, to reduce errors; thirdly the effective distance probed by adjacent modes should not be much less than that set by the photo- z error. The last of these is most easily effected with tomography, and the first two within 3D cosmic shear. 3D cosmic shear automatically deals (in principle) with the last constraint, through correlation of modes, but too finely-spaced modes may lead to near-singular covariance matrices. To deal with the first two constraints in tomography, the ℓ range chosen should be varied with shell.

The advantages of 3D cosmic shear are in being able to ensure that appropriate physical modes are analysed, in an integrated analysis of the entire sample. On the other hand tomography allows for a straightforward investigation of the redshift-dependence of the shear signal. Consequently we

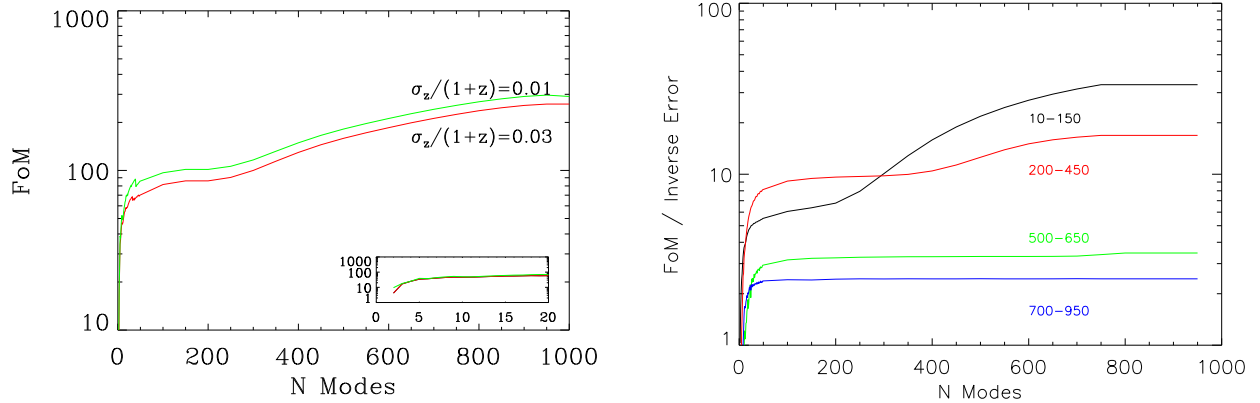


Figure 7. Left : We show the dark energy Figure of Merit (Albrecht et al., 2006) as a function of the number of k modes analysed. The lower/upper (red,green) lines are for $\sigma_z(z)/(1+z) = 0.03$ and 0.01 . The inset shows the change in FoM over the range of 2 to 20 bins for $\sigma_z(z)/(1+z) = 0.03$ (red, lower) and $\sigma_z(z)/(1+z) = 0.01$ (green, upper). This is for a Euclid wide survey (Refregier et al., 2010). We use a $\ell_{\max} = 5000$ and $k_{\max} = 1.5h\text{Mpc}^{-1}$. Right : For $\sigma_z(z) = 0.03$ we show how the FoM changes for particular ℓ ranges (labelled near each line). Note that in the full calculation, Figure 6, we use a range $\ell = 10\text{--}5000$, and that the largest contribution to the Fisher matrix $F_{ij} = \int d\ell \ell F_{\ell,ij}$ (equation 3) is in the range $\ell \approx 1000$ (Heavens et al., 2006).

conclude that both approaches have their advantages and it is sensible to do both.

Acknowledgements: We especially thank Rongmon Bordoloi for use of the photometric redshift estimates from Bordoloi et al., (2009) and Filipe Abdalla for use of redshift estimates from Abdalla et al., (2007) in an earlier draft. We thank Adam Amara for a careful reading of an early draft and an anonymous referee for many helpful comments. We also thank Andy Taylor and Fergus Simpson for many useful discussions. TDK is supported by a STFC Rolling Grant RA0888.

REFERENCES

- Albrecht, A., et al. 2006, arXiv:astro-ph/0609591
- Abdalla, F. B., Amara, A., Capak, P., Cypriano, E. S., Lahav, O., & Rhodes, J. 2008, MNRAS, 387, 969
- Amara, A., & Réfrégier, A. 2007, MNRAS, 381, 1018
- Amara, A., & Réfrégier, A. 2008, MNRAS, 391, 228
- Banerji, M., Ferreras, I., Abdalla, F. B., Hewett, P., & Lahav, O. 2010, MNRAS, 402, 2264
- Bernstein, G. M. 2009, Astro. Phys. Journal, 695, 652
- Bordoloi, R., Lilly, S. J., & Amara, A. 2009, arXiv:0910.5735
- Bridle, S., & King, L. 2007, New Journal of Physics, 9, 444
- Camera, S., Kitching, T. D., Heavens, A. F., Bertacca, D., & Diaferio, A. 2010, arXiv:1002.4740
- Castro, P. G., Heavens, A. F., & Kitching, T. D. 2005, Phys. Rev. D, 72, 023516
- Chevallier, M.; Polarski, D.; 2001, IJMPD, 10, 213
- Eisenstein, D. J., & Hu, W. 1999, Astro. Phys. Journal, 511
- Hannestad, S., & Wong, Y. Y. Y. 2007, Journal of Cosmology and Astro-Particle Physics, 7, 4
- Heavens, A. 2003, MNRAS, 343, 1327
- Heavens, A. F., Kitching, T. D., & Taylor, A. N. 2006, MNRAS, 373, 105
- Heavens, A. F., Kitching, T. D., & Verde, L. 2007, MNRAS, 380, 1029
- Heymans, C., & Heavens, A. 2003, arXiv:astro-ph/0310495
- Hu, W. 1999, Astro. Phys. Journal Letters, 522, L21
- Hu, W., & Jain, B. 2004, Phys. Rev. D, 70, 043009
- Jain, B., Connolly, A., & Takada, M. 2007, Journal of Cosmology and Astro-Particle Physics, 3, 13
- Jimenez, R., Kitching, T., Peña-Garay, C., & Verde, L. 2010, JCAP, 5, 35
- Joachimi, B., & Bridle, S. L. 2009, arXiv:0911.2454
- Joudaki, S., Cooray, A., & Holz, D. E. 2009, Phys. Rev. D, 80, 023003
- Kaiser, N. 1998, Astro. Phys. Journal, 498, 26
- Kitching, T. D., Heavens, A. F., Taylor, A. N., Brown, M. L., Meisenheimer, K., Wolf, C., Gray, M. E., & Bacon, D. J. 2007, MNRAS, 376, 771
- Kitching, T. D., Heavens, A. F., Verde, L., Serra, P., & Melchiorri, A. 2008, Phys. Rev. D, 77, 103008
- Kitching, T. D., Taylor, A. N., & Heavens, A. F. 2008, MNRAS, 389, 173
- Kitching, T. D., Amara, A., Abdalla, F. B., Joachimi, B., & Refregier, A. 2009, MNRAS, 399, 2107
- Kitching, T. D., & Taylor, A. N. 2010, arXiv:1005.2063
- Knox, L., Scoccimarro, R., & Dodelson, S. 1998, Physical Review Letters, 81, 2004
- Loverde, M., & Afshordi, N. 2008, Phys. Rev. D, 78, 123506
- Ma, Z., Hu, W., & Huterer, D. 2006, Astro. Phys. Journal, 636, 21
- Massey, R., Kitching, T., & Richard, J. 2010, arXiv:1001.1739
- Peacock, J. A., Schneider, P., Efstathiou, G., Ellis, J. R., Leibundgut, B., Lilly, S. J., & Mellier, Y. 2006, ESA-ESO Working Group on “Fundamental Cosmology”, Edited by J.A. Peacock et al. ESA, 2006.
- Refregier, A., Amara, A., Kitching, T., & Rassat, A. 2008, arXiv:0810.1285
- Refregier, A., Amara, A., Kitching, T. D., Rassat, A., Scaramella, R., Weller, J., & Euclid Imaging Consortium, f. t. 2010, arXiv:1001.0061
- Rudd, D. H., Zentner, A. R., & Kravtsov, A. V. 2008, Astro. Phys. Journal, 672, 19
- Schrabback, T., et al. 2009, arXiv:0911.0053
- Simon, P., King, L. J., & Schneider, P. 2004, AAP, 417, 873

- Smith, R. E., et al. 2003, MNRAS, 341, 1311
Taylor, A. N., Kitching, T. D., Bacon, D. J., & Heavens, A. F.
2007, MNRAS, 374, 1377
Tegmark, M., Taylor, A. N., & Heavens, A. F. 1997, Astro. Phys.
Journal, 480, 22
Thomas, S. A., Abdalla, F. B., & Weller, J. 2009, MNRAS, 395,
197

APPENDIX A: 3D COSMIC SHEAR

In this appendix we generalize the results of Heavens et al., (2006) and Kitching et al. (2007). We compute the covariance of the harmonic shear coefficients utilizing the individual posterior galaxy redshift probability distributions, rather than simplified sample properties (i.e. an averaged $p(z|z_p)$).

Starting with equation (1) we can begin to derive a theoretical expression for the expected coefficient values by linking the shear values to the Newtonian potential Φ via $\gamma = \frac{1}{2}\tilde{\partial}\tilde{\partial}\phi$ where ϕ is the lensing potential ($\tilde{\partial} = \partial_i + i\partial_j$) we can write a theoretical estimator like

$$\hat{\Gamma}_{ij}(k, \ell) = \left(\sum_g \sqrt{\frac{2}{\pi}} \phi_{j\ell}(kr_0^g) e^{-i\ell \cdot \theta^g} W(r_0^g) \right)_{ij}, \quad (15)$$

where $i, j = \{1, 2\}$ and $\hat{\gamma}_1(k, \ell) = \frac{1}{2}(\hat{\Gamma}_{11} - \hat{\Gamma}_{22})$ and $\hat{\gamma}_2(k, \ell) = \hat{\Gamma}_{12} = \hat{\Gamma}_{21}$.

The covariance of equation (15) can be written as

$$\langle \hat{\Gamma}(k_1, \ell_1) \hat{\Gamma}^*(k_2, \ell_2) \rangle = \sum_g \sum_h \left(\frac{2}{\pi} \right) j_{\ell_1}(k_1 r_0^g) j_{\ell_2}(k_2 r_0^h) \langle \phi \phi^* \rangle e^{-i\ell_1 \cdot \theta^g} e^{+i\ell_2 \cdot \theta^h} W(r_0^g) W(r_0^h) \quad (16)$$

where the covariance of the lensing potential can be written in terms of the Newtonian potential Φ (note we assume General Relativity and no anisotropic stress, so the Newtonian and curvature potentials are identical):

$$\langle \phi(r_0^g, \theta^g) \phi^*(r_0^h, \theta^h) \rangle = \frac{4}{c^2} \int_0^{r_0^g} dr' \int_0^{r_0^h} dr'' F_K(r^g, r') F_K(r^h, r'') \langle \Phi(r', \theta^g) \Phi^*(r'', \theta^h) \rangle \quad (17)$$

where $F_k(r, r') \equiv S_k(r - r') / [S_k(r) S_k(r')]$ ($S_k = \sinh(k), k, \sin(k)$ for open, flat or closed geometries so $F_k(r, r') = (r - r') / rr'$ for a flat universe). The real space Newtonian potential can also be written in terms of its spherical harmonic transform so that

$$\Phi(r, \theta^g) = \left(\frac{2}{\pi} \right)^{1/2} \int \frac{d^2 \ell}{(2\pi)^2} \int dk k j_\ell(kr^g) \Phi(k, \ell; t) e^{i\ell \cdot \theta^g}, \quad (18)$$

where t expresses the time-dependence. From now on we will identify this time dependence by an r dependence. Using Poisson's equation we can write the Newtonian potential's covariance (diagonal in ℓ because of isotropy) in terms of the matter power spectrum $P(k; r)$ as

$$\langle \Phi(r', \theta^g) \Phi^*(r'', \theta^h) \rangle = \left(\frac{2}{\pi} \right) A^2 \int \frac{dk}{k^2} \frac{j_\ell(kr') j_\ell(kr'')}{a(r') a(r'')} \sqrt{P(k; r') P(k; r'')} e^{-i\ell(\theta^h - \theta^g)} \quad (19)$$

where $A = 3\Omega_m H^2 / 2$. Note that, as shown in Castro et al. (2003) we take advantage of an algebraic convenience by using the geometric mean of the matter power spectra, this is well justified since at large separations (where the approximation may break down) any pair correlations are down weighted by the form of the Bessel functions.

This is fed into equations (15) then (16) so that we have an expression for the expected covariance of the 3D cosmic shear estimator

$$\begin{aligned} \langle \hat{\Gamma}_{ij}(k_1, \ell) \hat{\Gamma}_{ij}^*(k_2, \ell) \rangle &= \Delta\Omega \ell_i^2 \ell_j^2 \left(\frac{2}{\pi} \right)^2 \left(\frac{1}{c^2} \right) A^2 \sum_g \sum_h j_\ell(k_1 r_0^g) j_\ell(k_2 r_0^h) W(r_0^g) W(r_0^h) \\ &\int_0^{r_0^g} dr' \int_0^{r_0^h} dr'' F_K(r^g, r') F_K(r^h, r'') \int \frac{dk'}{k'^2} \frac{1}{a(r') a(r'')} j_\ell(k' r') j_\ell(k' r'') \sqrt{P(k'; r') P(k'; r'')}, \end{aligned} \quad (20)$$

the prefactor $\Delta\Omega$, the angular size or area of the survey, comes from final integrations over angle θ (see Kitching et al., 2007 for more information).

We use this final expression in Section 2.

APPENDIX B: TOMOGRAPHY FROM 3D COSMIC SHEAR

Here we derive the tomographic shear power spectra from the 3D cosmic shear covariance (equations 5, 6), assuming a global $\bar{p}(z|z_p)$.

We start with the full 3D cosmic shear power spectrum as a function of azimuthal ℓ and two radial k wavenumbers. This is an expansion of the equations (5) and (6):

$$C_{\ell}^{3D}(k_1, k_2) = \mathcal{A}^2 \int dr_g r_g^2 n(r_g) j_{\ell}(k_1 r_g) \int dr_h r_h^2 n(r_h) j_{\ell}(k_2 r_h) \int dr' \bar{p}(r'|r_g) \int dr'' \bar{p}(r''|r_h) \int d\tilde{r}' \int d\tilde{r}'' \frac{F_K(r', \tilde{r}')}{a(\tilde{r}')'} \frac{F_K(r'', \tilde{r}'')}{a(\tilde{r}'')'} \int \frac{dk'}{k'^2} j_{\ell}(k' \tilde{r}') j_{\ell}(k' \tilde{r}'') P^{1/2}(k'; \tilde{r}') P^{1/2}(k'; \tilde{r}'') \quad (21)$$

where we see that four Bessel functions enter the expression. The prefactor \mathcal{A}^2 is given by $\mathcal{A}^2 = \ell^4 \frac{4}{\pi^2 c^2} 9\Omega_m^2 H^4 / 4$. The $p(r[z]) = p(r[z]|r[z_p])$ is the redshift probability distribution, equivalent to $p(z|z_p)$ in equation (6), and we condense the notation here to match the literature for the tomographic case.

We now replace each Bessel function with its Limber approximated form (see equation 7) and find that we can rewrite the 3D power spectrum

$$C_{\ell}^{3D, \text{Limber}}(k_1, k_2) = \mathcal{A}^2 \left(\frac{1}{\ell}\right)^2 \left(\frac{\pi}{2\ell}\right)^2 \int d\tilde{r} \tilde{r}^2 \frac{P(\ell/\tilde{r}; \tilde{r})}{a^2(\tilde{r})} n(r_1) r_1^2 n(r_2) r_2^2 \int dr' \bar{p}(r') F_K(r', \tilde{r}) \int dr'' \bar{p}(r'') F_K(r'', \tilde{r}) \quad (22)$$

where we have introduced two radial distances r_1 and r_2 that are defined through the Limber approximation as $r_1 = \ell/k_1$ and $r_2 = \ell/k_2$. We can rewrite this in a more familiar form

$$C_{\ell}^{3D, \text{Limber}}(k_1, k_2) = \frac{9\Omega_m^2 H^4}{4c^2} \int dr \frac{P(\ell/r; r)}{a^2(r)} \frac{\mathcal{W}(r_1, r) \mathcal{W}(r_2, r)}{r^2} \quad (23)$$

where we define a weight factor as

$$\mathcal{W}(r_i, r) = [n(r_i) r_i^2] r \int dr' \bar{p}(r'|r_i) \frac{r - r'}{r'}. \quad (24)$$

We have written the geometric term in the flat geometry case for clarity $F_{K=0}(r, r') = (r - r')/rr'$, and the r^2 term cancels; to match convention we add a factor of r to the weight factor that must be cancelled by a r^2 denominator.

We note here that this expression is still a full 3D estimator in the Limber approximation. We use this expression in Section 4 to derive the tomographic power spectra and relate this to the 3D cosmic shear power spectra.

APPENDIX C: BIAS FOR SIGNAL IN THE COVARIANCE

The bias formalism presented in Knox et al. (1998), Amara & Refregier (2007) and Taylor et al. (2007) assumes that the parameter dependency comes through the mean of the signal. Here we show how the bias formalism can be extended to the case where the signal is in the covariance.

We start with a general expansion, in $\Delta\theta$, of the (log) likelihood about the maximum likelihood position $\theta_0 + \Delta\theta$

$$\mathcal{L}(\theta_0 + \Delta\theta) = \mathcal{L}(\theta_0) + \Delta\theta_i \partial_i \mathcal{L}(\theta_0) + \dots \quad (25)$$

where θ_0 in this case is the old position of the maximum likelihood and $\Delta\theta$ is the bias in parameters to a new maximum likelihood. By taking the derivative with respect to the parameters we have

$$\partial_j \mathcal{L}(\theta_0 + \Delta\theta) = 2\partial_j \mathcal{L}(\theta_0) + \Delta\theta_i \partial_i \partial_j \mathcal{L}(\theta_0) + \dots = 0 \quad (26)$$

where the log-likelihood is maximised at $\mathcal{L}(\theta_0 + \Delta\theta)$. By taking the expectation value of this and rearranging we find that the bias b_i in the i^{th} parameter can be written as

$$b_i = \Delta\theta_i = F_{ij}^{-1} \langle 2\partial_j \mathcal{L}(\theta_0) \rangle, \quad (27)$$

in a completely general way. Note that this makes the assumption that the Fisher matrix is unaffected to first order (this is a good approximation for small systematics as shown by Joachimi & Bridle, 2009).

By taking the result from Tegmark, Taylor & Heavens (1997) in the Gaussian case we can write the first derivative of the log-likelihood as

$$(2\mathcal{L}_{,i})_\ell = \text{Tr} [C_\ell^{-1} C_{\ell,i} - C_\ell^{-1} C_{\ell,i} C_\ell^{-1} D + C_\ell D_{,i}] \quad (28)$$

as a function of ℓ , where we replace $\partial_i = ,_i$. D is the data matrix $(x - \mu)(x - \mu)^t$. Here and for the remainder of this Appendix we assume an all sky survey such that the covariance C_ℓ is diagonal in ℓ (see Heavens et al., 2006; Kitching et al., 2007). We now assume that the mean is not a function of parameters and only consider the case where the parameters are in the covariance $D_{,i} = 0$; in the case that the signal is in the mean and $C_{\ell,i} = 0$ we recover the result of Amara & Refregier (2007) and Joachimi & Bridle (2009). Note that the quantity in the square brackets is a (ℓ, k, k') 3D matrix, and that the derivative of the log-likelihood is a function of ℓ .

To include a systematic we rewrite the covariance as some true covariance plus a systematic $C = C^t + C^s$. By taking the expectation value of equation (28) we have

$$\langle 2\mathcal{L}_{,i} \rangle_\ell = \text{Tr} [(C_\ell^t + C_\ell^s)^{-1} C_{\ell,i}^t - (C_\ell^t + C_\ell^s)^{-1} C_{\ell,i}^t (C_\ell^t + C_\ell^s)^{-1} \langle D \rangle] \langle 2\mathcal{L}_{,i} \rangle_\ell = \text{Tr} [(C_\ell^t + C_\ell^s)^{-1} C_{\ell,i}^t (I - (C_\ell^t + C_\ell^s)^{-1} C_\ell^t)] \quad (29)$$

where the expectation of the data is the true covariance $\langle D \rangle = C_\ell^t$. Finally we note that the total log-likelihood is in general a sum over $\ell = (\ell_x, \ell_y)$ modes $\mathcal{L} = \sum_{\ell_x, \ell_y} \mathcal{L}_{\ell_x, \ell_y}$, so a similar summation must be performed over the derivatives of the log-likelihood. For the Fisher matrix and for the bias here we write this summation as an integral over the modulus $\ell = |\ell|$, and account for the density of state in (ℓ_x, ℓ_y) (see Appendix B in Kitching, Taylor, Heavens, 2007).

We can now write an expression for the bias caused by a systematic function in the case of the parameters being in the covariance like

$$b_i = F_{ij}^{-1} \left\{ g \int d\phi_\ell \int d\ell \ell \text{Tr} [(C_\ell^t + C_\ell^s)^{-1} C_{\ell,j}^t (I - (C_\ell^t + C_\ell^s)^{-1} C_\ell^t)] \right\}. \quad (30)$$

In this final step we have also added an integration over ℓ -space where g is the density of states in ℓ ; this is exactly the same integration that is performed when calculating the Fisher matrix (see Appendix B in Kitching, Taylor, Heavens, 2007). If the systematic is very low $|C^s| \ll C^t$ then $\langle 2\mathcal{L}_{,i} \rangle = 0$ and the bias is effectively zero.